Article

Influenza A Virus Infection Alters Lipid Packing and Surface Electrostatic Potential of the Host Plasma Membrane

Annett Petrich [ID] **and Salvatore Chiantia *** [ID]

Institute of Biochemistry and Biology, University of Potsdam, Karl-Liebknecht-Str. 24–25,
14476 Potsdam, Germany
* Correspondence: chiantia@uni-potsdam.de

Abstract: The pathogenesis of influenza A viruses (IAVs) is influenced by several factors, including IAV strain origin and reassortment, tissue tropism and host type. While such factors were mostly investigated in the context of virus entry, fusion and replication, little is known about the viral-induced changes to the host lipid membranes which might be relevant in the context of virion assembly. In this work, we applied several biophysical fluorescence microscope techniques (i.e., Förster energy resonance transfer, generalized polarization imaging and scanning fluorescence correlation spectroscopy) to quantify the effect of infection by two IAV strains of different origin on the plasma membrane (PM) of avian and human cell lines. We found that IAV infection affects the membrane charge of the inner leaflet of the PM. Moreover, we showed that IAV infection impacts lipid–lipid interactions by decreasing membrane fluidity and increasing lipid packing. Because of such alterations, diffusive dynamics of membrane-associated proteins are hindered. Taken together, our results indicate that the infection of avian and human cell lines with IAV strains of different origins had similar effects on the biophysical properties of the PM.

Keywords: fluorescence microscopy; spectral imaging; quantitative microscopy; fluorescence correlation spectroscopy; fluorescence resonance energy transfer; biosensors; plasma membrane; membrane fluidity; lipid packing; influenza A virus

1. Introduction

Influenza A virus (IAV) is an enveloped, negative-sense RNA virus that belongs to the Orthomyxoviridae family [1,2]. This pathogen poses a significant threat to both humans and animals and can cause widespread infections resulting in significant morbidity and mortality [2,3]. Apart from the commonly occurring seasonal IAV subtypes H1N1 and H3N2, there has been a recent rise in human infections caused by different avian influenza viruses such as H5Nx, H7N9, and H9N2, as well as swine influenza viruses [2,3]. Several studies have revealed that IAV infection can alter the lipid metabolism in various hosts, impacting IAV replication, viral envelope lipid composition and potentially contributing to pathogenicity [1,4–9]. These alterations have been also linked to inflammatory responses in host organisms [1,8]. Additionally, some avian IAV strains have been found to trigger a more intense inflammatory response in humans compared to human(-adapted) strains [10–12]. Therefore, investigating the connection between lipid metabolism, the physical properties of cellular membranes, and IAV infection is crucial for understanding the pathogenic mechanisms of IAV and developing targeted antiviral treatments.

In general, lipids and cellular membranes play a crucial role in various stages of the IAV life cycle, such as virus–host receptor interaction, membrane fusion, nuclear transport, virion assembly, and budding [11,13–17]. Several studies have proposed that IAV assembles and buds from specific lipid domains within the apical plasma membrane (PM), which are enriched in cholesterol and sphingolipids [15,16,18–21]. This hypothesis is supported by lipidome analyses conducted on purified influenza viral envelopes, which were shown

to contain higher levels of certain sphingolipid species and cholesterol, thus potentially increasing the bilayer structural order in comparison to the host cell membrane [5,19,21,22]. Furthermore, removing cholesterol from the viral envelope has been found to destabilize the viral membrane and morphology, leading to a decrease in virus infectivity [23,24]. Of note, a previous study found that three egg-grown IAV strains with varying pathogenicity exhibited a modified glycerophospholipid (GPL) composition compared to non-infected allantoic fluid (NAF) or mammalian cells [5]. Specifically, highly pathogenic IAV strains were found to contain higher fractions of sphingomyelin (SM) and saturated fatty acids compared to the other IAV strains and NAF [5].

On the other hand, it is also well established that IAV structural proteins participate in specific lipid–protein interactions in infected cells. For example, the spike proteins, hemagglutinin (HA) and neuraminidase (NA) are transported to the PM via cholesterol-/sphingomyelin-rich vesicles [13,14,17,18,20,25,26] and their lateral organization might be indirectly influenced by lipids [27,28] or specifically depend on ordered lipid–protein domains [20,29,30]. The cytoplasmic tail of HA possesses multiple basic residues which interact with phosphoinositides (e.g., PIP2), modulating protein clustering and membrane association [31,32]. Additionally, several studies have investigated the interplay between lipids and the IAV matrix protein 2 (M2) [30,33–40]. It has been proposed that M2 is transported to the apical PM independently from HA and NA through its interaction with the phosphatidylserine (PS)-conjugated, microtubule-associated protein 1 light chain 3 protein (LC3-II) [37,41–43]. Thus, the interaction between M2 and the IAV matrix protein 1 (M1) might be supported by a local enrichment of PS at the virus assembly site [44–46]. Moreover, previous studies have indicated that M2–M2 interactions are enhanced in cholesterol-enriched membranes [35,39,40].

These findings emphasize the crucial role of a controlled lipid metabolism in multiple stages of IAV infection, which appears to be influenced by both the origin of the IAV strain and the host type [1,4–11,14,17,47]. While previous studies have primarily investigated virus entry, fusion, and replication, a comprehensive analysis of how the host environment and IAV strain origin impact virus assembly and the PM environment in general is still lacking. Previous lipidomic studies focused mainly on the analysis of purified influenza virions [5,19,21,22] and only few analyzed the lipidome of whole (non-)infected mammalian cells [6,7,9,22]. A small number of studies observed no significant difference in the lipidome of whole cells after infection compared to non-infected cells, whereas others reported IAV-mediated induction of sphingomyelin, cholesterol, and fatty acid biosynthesis [6,7,9,22].

In light of these contrasting results, we directly investigated in this work the physical properties of the PM lipid bilayer, comparing infected and non-infected cells. To this aim, we used avian and human IAV strains, as well as two cell lines. The previously observed increase of the transport of cholesterol-/sphingolipid-rich vesicles [48] and GPL-conjugated LC3-positive vesicles [37,41–43] to the PM and their subsequent fusion with the PM might have an impact on membrane organization, composition, fluidity and membrane protein dynamics. For this reason, we used a fluorescence membrane charge sensor (MCS) to monitor changes in the electrostatic potential at the inner leaflet of the membrane [49]. Second, we quantified the influence of IAV infection on PM fluidity by using solvatochromic dyes (Laurdan and Di-4ANEPPDHQ) which are influenced by lipid packing, membrane hydration, and lipid composition [50,51]. Finally, we applied scanning fluorescence spectroscopy (sFCS) to monitor the dynamics of different membrane-associated proteins [52–55]. Our findings indicate that infection by either IAV strains might modulate the lipid composition of the PM and lipid–lipid interactions in both cell models. These changes in membrane properties have a direct effect also on membrane protein dynamics.

2. Materials and Methods

2.1. Plasmids

The plasmid for FRET analysis, MCS+ [49], was acquired from Addgene (gift from Katharina Gaus, Addgene plasmid #90412). All plasmids for sFCS analysis encoded

the monomeric enhanced green fluorescent protein (mEGFP), which was fused to the C-terminus of a myristoylated and palmitoylated peptide (mp-mEGFP), avian influenza A/FPV/Rostock/1934 virus hemagglutinin (HA-mEGFP, Addgene plasmid #127810), or to the N-terminus of a glycosylphosphatidylinositol (GPI)-anchor (GPI-mEGFP, Addgene plasmid #182866) and were previously described [42,56]. A schematic overview of the localization of each construct within the PM is provided Figure S1A,F.

2.2. Cell Culture, Transfection and Infection

Madin-Darby canine kidney type II (MDCK II) cells (ECACC 00062107, European Collection of Authenticated Cell Cultures, Porton Down, UK), chicken embryonic fibroblast cell line DF1 (ATCC number: CRL–12203, kindly provided by Andreas Herrmann, Humboldt University Berlin, Germany) and human embryonic kidney (HEK) cells from the 293T line (CRL-3216TM, purchased from ATCC, Kielpin Lomianki, Poland) were maintained in phenol red-free, high glucose Dulbecco's modified Eagle's medium (DMEM) supplemented with 2 mM L-glutamine, 100 U/mL penicillin, 100 µg/mL streptomycin and 10% fetal bovine serum in a humidified incubator at 37 °C and 5% CO_2 atmosphere. Cells were passaged every 2–4 days until passage 15. All cell culture products were purchased from PAN-Biotech (Aidenbach, Germany).

For imaging experiments, 35 mm dishes (CellVis, Mountain View, CA, USA) with an optical glass bottom (#1.5 glass, 0.16–0.19 mm) were coated with 0.01% (w/v) poly-L-lysine (molecular weight [MW] 150,000–300,000 Da, Sigma-Aldrich, Munich, Germany) for four hours at 37 °C and rinsed three times with Dulbecco's phosphate-buffered saline containing Mg^{2+}/Ca^{2+} ($DPBS_{+/+}$; PAN-Biotech, Aidenbach, Germany) before cell seeding. Cells were seeded 24 h prior to transfection and infection at a density of 6×10^5 cells per dish.

For FRET and sFCS measurements, cells were transfected four hours prior infection with Turbofect® according to the manufacturer's protocol (Thermo Fisher Scientific, Waltham, MA, USA) by using 100 ng pDNA per dish for the membrane-associated proteins (mp-mEGFP and GPI-mEGFP) and the FRET-sensor (MCS+) or 600 ng pDNA per dish for the transmembrane glycoprotein, HA-mEGFP. Briefly, pDNA was pre-incubated with 2 µL of reagent in a final volume of 50 µL serum-free medium and was added dropwise to cells after incubation for 20 min at room temperature.

Before single-round infections with the avian influenza A/FPV/Rostock/1934 virus mutant 1 (FPV, H7N1, kind gift from Michael Veit, Free University Berlin [57]) and the human influenza A/WSN/1933 virus (WSN, H1N1, kind gift from Andreas Herrmann, Humboldt Universität zu Berlin, Germany), cells were washed three times with $DPBS_{+/+}$ and then infected with a multiplicity of infection (MOI) 5 in DMEM containing 0.2% (w/v) Bovine Serum Albumin (BSA; Sigma Aldrich, Taufkirchen, Germany), 2 mM L-glutamine, 100 U/mL penicillin, and 100 µg/mL streptomycin. Cells were first incubated for 15 min on ice and then for 45 min in a humidified incubator at 37 °C and 5% CO_2 atmosphere. Afterwards, cells were rinsed three times with $DPBS_{+/+}$ and fresh infection medium was added. Cells were further maintained under standard growth conditions until the measurements (~16 h post infection (hpi)). This time point has been chosen in agreement with previous studies (monitoring infection after 12, 18 and 24 h [7]) and also with our results, showing that M1 is efficiently recruited to the PM after ca. 16 h [46]. Virus propagation and titration were performed in MDCK II cells as previously described [46].

2.3. Alteration of PM Properties to Obtain Control Samples

For FRET measurements, cells were treated with lipid vesicles containing the anionic phospholipid 1,2-dioleoyl-sn-glycero-3-phospho-L-serine (DOPS, purchased from Avanti Polar Lipids, Inc., Alabaster, AL, USA) to increase the concentration of negative-charged lipids at the PM and, thus, function as positive control [49]. Lipids were dissolved in chloroform at the concentration of 1 mM, dried on the walls of a glass vials under nitrogen gas and stored at −20 °C until use. Prior to each experiment, the lipid film was rehydrated with DPBS without Ca^{2+}/Mg^{2+} ($DPBS_{-/-}$) to a final concentration of 0.1 mM and vigorously

vortexed until multilamellar vesicles (MLV) were formed. The MLV suspension was then sonicated to clarity in a bath sonicator to form small unilamellar vesicles (SUVs). DOPS vesicles were added to the cells after three washing steps with DPBS$_{-/-}$ and incubated for 30 min at room temperature. Afterwards, cells were washed with DPBS$_{-/-}$ and fresh culture medium was added before starting the measurement.

For *GP* measurements, cells were treated with 10 mM methyl-beta cyclodextrin (MbCD; Sigma-Aldrich, Darmstadt, Germany) in serum-free DMEM after three washing steps with DPBS$_{+/+}$ to obtain a control sample featuring an increase in membrane fluidity, consequent to cholesterol depletion. After incubation for four hours in a humidified incubator at 37 °C and 5% CO_2 atmosphere, cells were washed three times with DPBS$_{+/+}$ before labelling with a fluorophore.

2.4. Membrane Labelling with Laurdan and Di-4-ANEPPDHQ

The membrane probes, Di-4-ANEPPDHQ and Laurdan (6-dodecanyl-2-dimethylamin-onaphtalene), were obtained from Molecular Probes (Eugene, OR, USA) and dissolved in ethanol and dimethyl sulfoxide (DMSO, Sigma-Aldrich, Darmstadt, Germany) at the desired concentrations, respectively. Aliquots of 2 mM stock solutions were stored at −20 °C until use. Before each experiment, membrane probes were diluted in serum-free and phenol red-free DMEM to a final concentration of 1 μM for Di-4-ANEPPDHQ and 5 μM for Laurdan (the final concentration of DMSO was kept below 0.5% *v/v*). The probes were added to the cells after three washing steps with DPBS$_{+/+}$ and incubated for 10 min at room temperature. Afterwards, cells were washed twice with DPBS$_{+/+}$, and fresh serum-free and phenol red-free DMEM were added to the cells before imaging.

2.5. Confocal Spectral Imaging

Spectral imaging was performed on a Zeiss LSM 780 system (Carl Zeiss Microscopy GmbH, Oberkochen, Germany) equipped with a Plan-Apochromat 40×/1.2 Korr DIC M27 water immersion objective and a 32-channel gallium arsenide phosphide (GaAsP) detector array. The excitation sources were a 405 nm diode laser (for Laurdan) and a 488 nm Argon laser (for Di-4-ANEPPDQH and the FRET-sensor). Images were collected with detection ranges between for 419 and 610 nm for Laurdan and 499 and 695 nm for Di-4-ANEPPDQH and FRET-sensor in 8.9 nm increments after passing 405/625 nm or 488 nm dichroic mirrors, respectively. Laser power was adjusted so that no pixel saturation occurred. For image acquisition, 10 frames were taken with a frame resolution of 128 × 128 pixels, a pixel dwell time of 50.4 μs, and a pinhole size of 1 AU to reduce out-of-focus fluorescence. All measurements were performed at room temperature (22 ± 1 °C) and images were acquired at the equatorial plane of the cell.

2.6. FRET Analysis

Confocal spectral images were analyzed as previously described [42,49,58]. Briefly, for each experimental condition, ca. 18–30 confocal images were acquired. To quantify the FRET signal, several regions of interest (ROIs) were manually defined within well-defined regions of the PM (e.g., outside cell–cell contacts), directly on mean (*n* = 10 frames) intensity maps. It is worth noting that the ROI selection was performed before and independently from the *RG* ratio calculations. Emission spectra were then computed from the mean normalized fluorescence intensities over all pixels of each ROI, after the application of an intensity threshold (set as 1/5 of the maximum intensity over all wavelengths). Additionally, the normalized pixel intensity values within the ROIs were used to calculate the red–green intensity ratio (*RG* ratio). The red spectral range was set 601–619 nm and the green from 512–539 nm. Hence, the *RG* ratio is defined as:

$$RG \text{ ratio} = \frac{\sum_{601\text{ nm}}^{619\text{ nm}} I}{\sum_{512\text{ nm}}^{539\text{ nm}} I}. \tag{1}$$

RG ratio values were then either plotted as *RG* ratio maps or used for the normalized occurrence histograms of all selected pixels. The *RG* ratio distributions for these samples range from 0 to ca. 1, corresponding to low to high FRET levels. A schematic overview of the FRET analysis is provided in Figure S1A,B.

All calculations were performed using a custom-written MATLAB code (The Math-Works, Natick, MA, USA). The mean normalized intensity spectra were visualized by using GraphPad Prism vs. 9.0.0 (GraphPad Software, LCC, San Diego, CA, USA).

2.7. GP Index Analysis

Spectral *GP* measurements were analyzed as previously described [42,54,58]. Briefly, for each experimental condition, ca. 14–40 confocal images were acquired. First, an average fluorescence intensity image ($n = 10$ frames) was calculated. This average intensity map was used for defining multiple ROIs containing isolated regions of the PM (e.g., outside cell–cell contacts). It is worth noting that the ROI selection was performed before and independently from the *GP* value calculations. After the application of an intensity threshold (set as 1/5 of the maximum intensity over all wavelengths), pixel intensities of each channel were used to calculate the average fluorescence intensity spectrum over all pixels within this mask. Moreover, the generalized polarization (*GP*) index was calculated from a pixel-wise analysis and the obtained values were used to obtain the *GP* map, the normalized occurrence histograms of all selected pixels and to compute the average *GP* value over the entire ROI. For the calculation of the *GP* values, the wavelengths relative to ordered and disordered phases were previously identified for each probe, by measuring standard giant unilamellar vesicles (GUVs, Figure S1E). In this study, spectral ranges of 420–450 nm (with enhanced emission from ordered bilayers) and 520–560 nm (showing enhanced emission for disordered bilayers) were set for Laurdan. 545–585 nm and 625–690 nm were chosen for Di-4-ANEPPDQH. The sum of the normalized intensity values for each range (I_o and I_d, respectively) was then used for the *GP* index calculation as follows:

$$GP \text{ index} = \frac{\sum I_o - \sum I_d}{\sum I_o + \sum I_d}. \tag{2}$$

The *GP* index ranges from -1.0 (very fluid) to 1.0 (gel-like). A schematic overview of the *GP* index analysis is provided in Figure S1C–E.

All measurements were analyzed with custom-written MATLAB code (The Math-Works, Natick, MA, USA). The mean normalized intensity spectra were visualized by using GraphPad Prism vs. 9.0.0 (GraphPad Software, LCC, San Diego, CA, USA).

2.8. sFCS Analysis

Scanning FCS experiments were performed on a Zeiss LSM780 system (Carl Zeiss Microscopy GmbH, Oberkochen, Germany) as previously described [54,56,59]. Briefly, the samples were excited with 488 nm Argon laser ($\approx$3 μW) through a Plan-Apochromat $40\times$/1.2 Korr DIC M27 water immersion objective. The fluorescence signal was collected between 499 and 600 nm with a 32-channel GaAsP detector array after passing through a 488 nm dichroic mirror. The pinhole size was restricted to an airy unit of one to minimize out-of-focus signal. Line scans of 256×1 pixels and pixel size $\approx$ 80 nm were acquired perpendicular to the PM with a scan time of 472.73 μs. Typically, 400,000 lines were acquired in photon counting mode. All measurements were performed at 22 ± 1 °C.

Prior to each experiment, the confocal volume was calibrated by performing a series of point FCS measurements with a 30 nM Alexa Fluor® 488 solution (AF488, Thermo Fischer, Waltham, MA, USA) at the same excitation power and beam path used for sFCS measurements. For that, the fluorescence signal was optimized at first by adjusting the collar ring of the objective and the pinhole position to the maximal count rate. Then, FCS measurements (15 repetitions of 10 s) at five different positions were performed and the data was fitted using a 3D diffusion model including a triplet contribution in order to calculate the structure parameter S (ratio of the vertical and lateral dimension of the

confocal volume, typically between 6 and 8) and the diffusion time τ_d (usually, $\approx 30 \pm 2$ µs). The measured average diffusion time and a previously determined diffusion coefficient ($D_{488} = 435$ µm^{2}s^{-1}) [60] were used to calculate the waist ω_0 of the confocal volume (usually, $\approx 230 \pm 10$ nm).

Scanning FCS data were exported as TIFF files, imported and analyzed in MATLAB (Version 2020a, The MathWorks, Natick, MA, USA) using a custom code as previously described [46,54,56]. Briefly, all scanning lines were aligned and divided into blocks in which the lines were fitted with a Gaussian function in order to define the membrane position. Subsequently, pixels of each line were integrated to provide the membrane fluorescence time series $F(t)$. Photobleaching was corrected by a two-component exponential fit function [61]. Afterwards, the normalized autocorrelation function (ACF) was calculated using the following Equations (3) and (4):

$$G(\tau) = \frac{\langle \delta F(t) \delta F(t + \tau) \rangle}{\langle F(t) \rangle^2} \tag{3}$$

where

$$\delta F = F(t) - \langle F(t) \rangle. \tag{4}$$

The ACF was calculated segment wise (each ca. 20 s long) and segments with extreme alterations were removed before averaging the ACFs. Finally, a two-dimensional diffusion fitting model and the structure parameter S from the calibration were used to analyze the ACF [62], as described in Equation (5):

$$G(\tau) = \frac{1}{N}\left(1 + \frac{\tau}{\tau_D}\right)^{-\frac{1}{2}}\left(1 + \frac{\tau}{\tau_D S^2}\right)^{-\frac{1}{2}} \tag{5}$$

where τ_D represents the diffusion time and N the number of particles. The diffusion coefficient D was then calculated using the waist ω_0 from the calibration as follows:

$$D = \frac{\omega_0^2}{4\tau_D} \tag{6}$$

A schematic overview of the sFCS analysis is provided in Figure S1G.

2.9. Statistical Analysis

Data from at least two independent experiments were pooled, analyzed, and visualized using a self-written R script (R Foundation for Statistical Computing, Vienna, Austria) built from common packages (rstatix, fBasics, ggplot2 and ggpubr). Data are displayed as box plots with single data points corresponding to measurements in single cells. Median values and whiskers ranging from minimum to maximum values are displayed. The corresponding descriptive statistics for each plot are summarized in supplementary tables (see Supplementary Materials). The *p* values are provided in each graph and figure captions. Statistical significance was tested by using D'Agostino-Pearson normality test followed by one-way ANOVA analysis and Tukey's multiple comparisons test.

3. Results

3.1. Infection Increases the Negative Surface Charge of the Inner Leaflet of the PM

Previous studies have shown that the viral proteins, HA and M1, can modulate the clustering of PIP2 in the PM [31,32]. Moreover, it was reported that the apical transport of M2 is carried out via PS-conjugated LC3-positive vesicles [41–43,63]. Both observations could have an impact on the membrane composition and, specifically, the amount and lateral organization of anionic lipids.

First, we investigated to what extent the infection induced apoptosis which, in turn, could lead to PS flipping to the outer leaflet of the membrane, as it was reported for late infection states [64,65]. Trans-bilayer rearrangement of PS might in fact influence the

quantification of membrane charge distribution [66,67]. We have therefore characterized the state of the cells using PI and Annexin V to determine cell viability and apoptosis-induced PS flipping to the outer leaflet of the PM [64,67]. Infection status and total cell numbers were determined via immunofluorescence and Hoechst 33,342 staining, respectively (Figure S2, Table S1). We used H_2O_2/Saponine-treated cells as positive control for apoptosis and cell death [68,69]. The FPV infection efficiencies in HEK293T and DF1 samples were $81.9 \pm 4.9\%$ and $64.7 \pm 8.3\%$ (mean $\pm$ SD). The values for WSN were $90.6 \pm 3.6\%$ and $83.1 \pm 14.7\%$ (mean $\pm$ SD) (Figure S2A,B,E). We observed no significant induction of apoptosis or PS translocation 16 h after infection with FPV or WSN, in either cell line (Figure S2A–D).

Next, we used a fluorescence membrane charge sensor (MCS+) to monitor changes of the electrostatic potential at the inner leaflet of the membrane [49] in non-infected (MOCK), FPV-/WSN-infected and DOPS-SUV-treated HEK293T and DF1 cells (Figure 1).
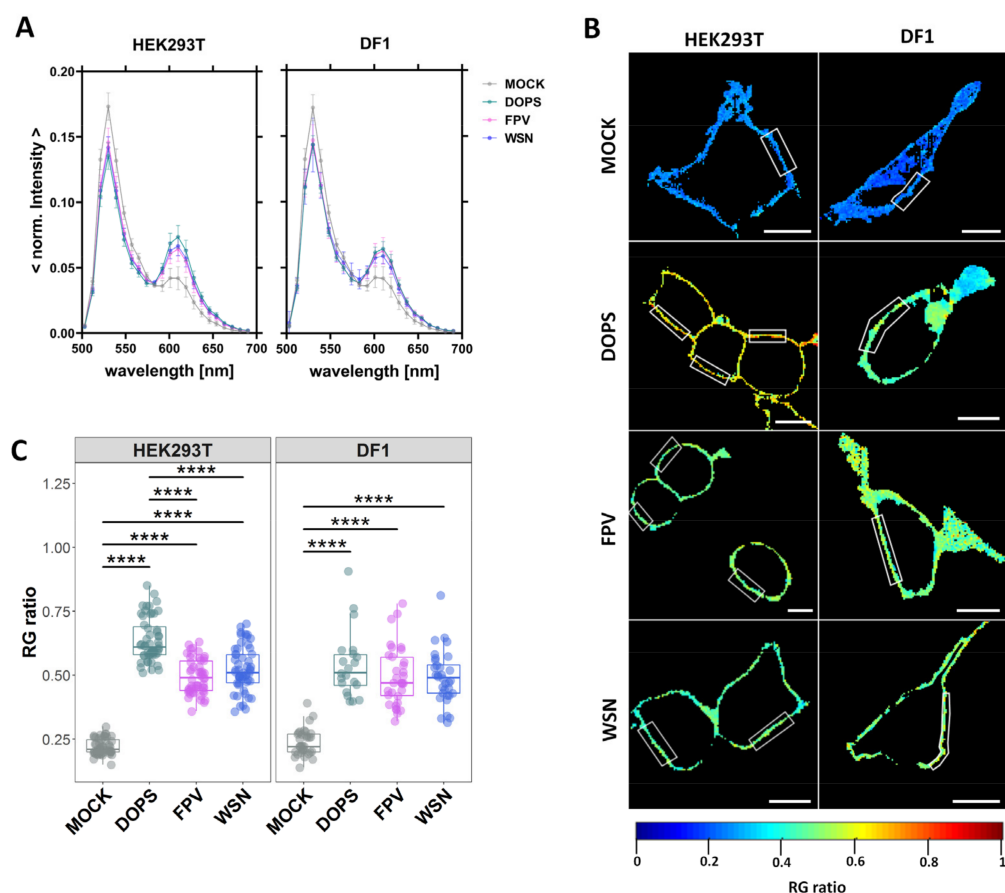

Figure 1. Increase of negative surface charge at the inner leaflet of the PM in infected cells. HEK293T and DF1 cells were either: non-infected (MOCK), treated with DOPS-SUV (DOPS, positive control), infected with FPV or with WSN influenza A strains. All cells were expressing the FRET-sensor MCS+ and emission spectrum images (22 spectral channels from 499 nm to 695 nm) were acquired 16 hpi using 488 nm excitation. (**A**) Average normalized emission spectra of all the selected regions of interest (ROI) at the equatorial plane of HEK293T and DF1 cells expressing MCS+, following the indicated treatment. Data are represented as mean $\pm$ SD from 50–55 HEK293T cells and 21–33 DF1 cells from two independent experiments. (**B**) Representative ratiometric FRET images (*RG* ratio, pseudo-colored as indicated by the color scale) of HEK293T and DF1 cells expressing MCS+. White rectangles represent examples of ROIs at the PM selected for FRET quantification. Scale bars represent 10 µm. (**C**) *RG* ratio derived from the average intensity spectra of each cell type for the indicated treatment. Data from two separate experiments were pooled, plotted, and analyzed using a one-way ANOVA Tukey's multiple comparison test (**** $p < 0.0001$). Each data point represents the average value measured for a ROI at the PM in one cell (Table S2).

FRET measurements to quantify the membrane potential were carried-out via spectral imaging, instead of the standard, filter-based method [49]. The spectral imaging approach and detection in the photon-counting mode were previously shown to provide more information and to improve the accuracy and sensitivity of the measurements [70,71]. For the FRET analysis, ROIs at the equatorial plane of isolated membrane regions were chosen within the average intensity map and the *RG* ratio was quantified via the spectral information from each pixel. High *RG* ratio values correspond to a relative higher fluorescence emission peak in the longer-wavelength region (i.e., more efficient FRET between the MCS+ domains) and, therefore, a higher negative membrane potential at the inner leaflet of the membrane. We used DOPS-treated cells as a positive control, since it was shown that DOPS is quickly internalized and transported to the inner leaflet of the PM with a half time of a few minutes [72,73]. The sensor MCS+ was expressed with similar efficiency in all cell lines and differently treated samples. For both cell lines, we observed an increase of the second emission maximum upon virus infection or DOPS-SUV-treatment (Figure 1A), which resulted in ~2-fold higher *RG* ratio values (Figures 1B,C and S3, Table S2). Interestingly, no significant differences between IAV strains or cell types were detectable. In summary, these findings indicate a significant increase of the available negative charge at the inner leaflet of the PM in FPV- and WSN- infected cells, independent of their host cell type.

3.2. IAV Infection Increases Lipid Packing in the Plasma Membrane Lipid Bilayer

Multiple studies have shown that the membrane of influenza A virions contains high levels of sphingolipids and cholesterol, a modified GPL composition and is more ordered compared to the host cell membrane [5,7,19,21,22,74,75]. Little is known about alterations in the physical properties (e.g., order, lipid packing) of the host cell membrane. Therefore, we investigated the effect of IAV infection on membrane order directly in the PM of living cells, using solvatochromic probes (i.e., Laurdan and Di-4ANEPPDHQ). The spectroscopic properties of these dyes depend on the local membrane environment [50,51]. Specifically, their emission spectra exhibit a blue-shift when they localize in an ordered, more apolar environment, such as a liquid-ordered phase or a "lipid-raft" domain [50,51]. This shift can be quantified by calculating the *GP* value, which involves a ratiometric analysis of the fluorescence intensity in two spectral regions [58]. Higher *GP* values indicate a higher fluorescence intensity in the shorter-wavelength region, which corresponds to a higher degree of membrane order and lipid packing [51].

We used GUVs with varying lipid compositions as reference for the behavior of each dye in solid ordered gel ($L_ß$) phase and liquid-disordered (L_d) phase membranes. With such reference samples, we could reliably test our experimental conditions, the *GP* analysis pipeline, and the phasor approach (Figures S1E and S4). DLPC GUVs (consisting of a bilayer in the L_d phase) were significantly distinguishable from DPPC GUVs (bilayer in the $L_ß$ phase), using either Laurdan or Di-4-ANEPPDHQ. In agreement with previous reports, the spectral shift of Di-4-ANEPPDHQ is less dramatic than that observed for Laurdan [50,58,76–78].

The investigation of changes in lipid packing was carried out in non-infected cells (MOCK), FPV- and WSN-infected cells and MbCD-treated cells (Figures 2, S5 and S6, Tables S3 and S4). MbCD-treated cells were used as control, since it is known that cholesterol depletion reduces membrane order [58,67]. In all cases, PM regions at the equatorial plane of the cells were chosen within the average intensity map and the *GP* index was quantified from the spectral information of each pixel. We observed in both cell lines a shift in fluorescence emission towards the shorter-wavelength region upon FPV- and WSN-infection (Figure 2A,D). This shift was less pronounced in Di-4-ANEPPDHQ- stained cells, in agreement with control experiments in GUVs (Figure S4).
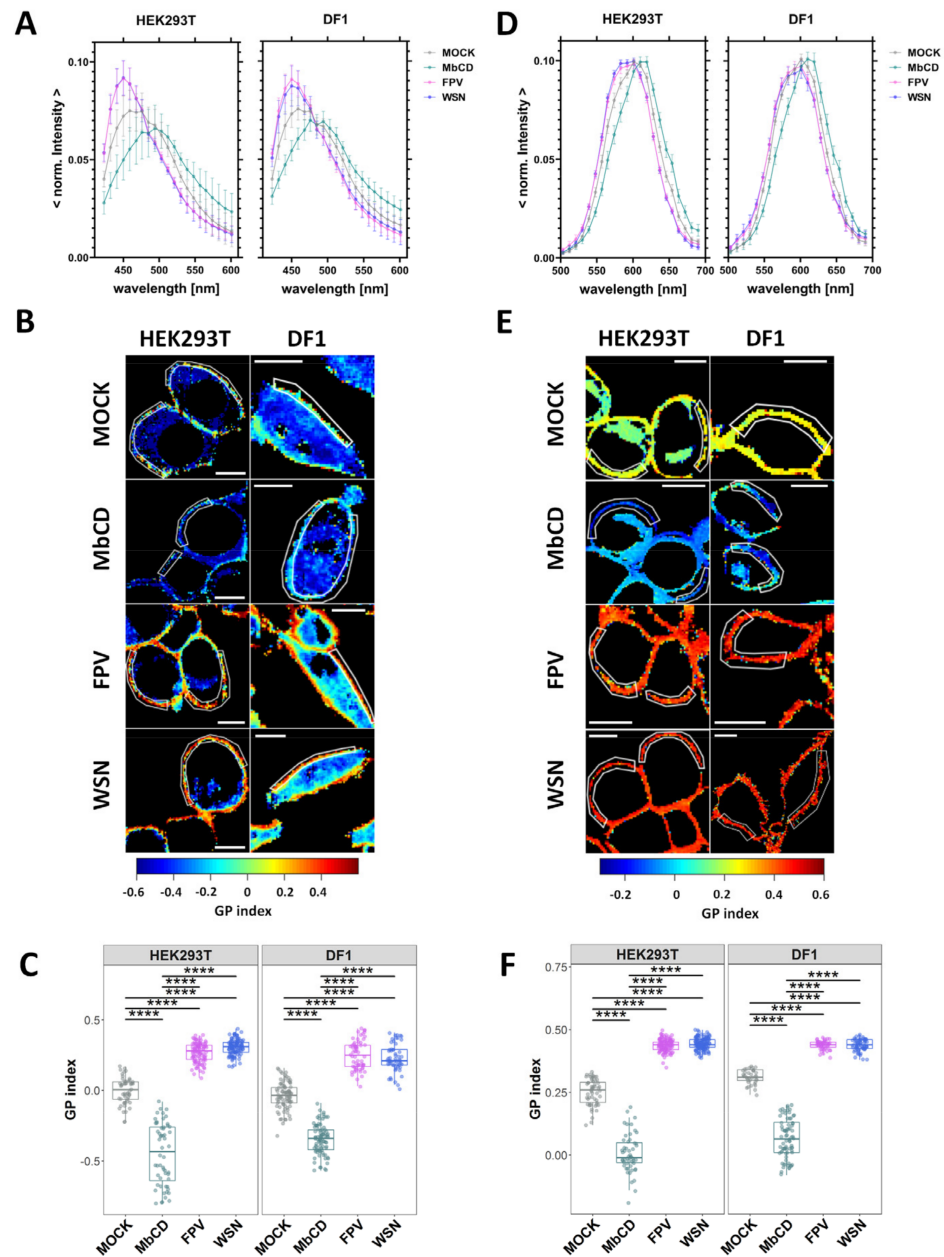
Figure 2. Increase of lipid packing of the PM upon IAV infection. HEK293T and DF1 cells were either non-infected (MOCK), treated with methyl-β-cyclodextrin (MbCD), infected with FPV or with WSN influenza A strains. All cells were labelled with the solvatochromic probes Laurdan (**A**–**C**) and Di-4-ANEPPDHQ (**D**–**F**), and then imaged 16 hpi. Averaged, normalized fluorescence emission spectra of all selected regions of interest (ROI) at the equatorial plane of HEK293T and DF1 cells stained with Laurdan (**A**) or Di-4-ANEPPDHQ (**D**), for the indicated treatment. Data are represented as mean ± SD of 52–110 cells stained with Laurdan and 36–127 cells stained with Di-4-ANEPPDHQ from three independent experiments (Tables S3 and S4). Representative ratiometric *GP* images (*GP* index, pseudo-colored as indicated by the color scale) of HEK293T and DF1 cells stained with Laurdan (**B**) or Di-4-ANEPPDHQ (**E**). White lines represent examples of ROIs at the PM selected for *GP* index quantification. Scale bars represent 10 μm. *GP* index derived from the average intensity spectra from Laurdan- (**C**) or Di-4-ANEPPDHQ-stained (**F**) cells for each cell type and indicated treatment. Data from three separate experiments were pooled, plotted, and analyzed using one-way ANOVA Tukey's multiple comparison test (**** $p < 0.0001$). Each data point represents the average value measured for a ROI at the PM in one cell (Tables S3 and S4).

MbCD-treated cells showed as expected, for all cell types, a red-shifted spectrum [58,67]. Moreover, the alternative representation via phasor plots showed a clear "clockwise" shift (see also Figure S4C) for infected cells (Figure S5), confirming stronger lipid–lipid interactions in these samples. Finally, our data indicate that the observed PM ordering effect consequent to IAV infection does not depend on IAV strain, cell type, or the degree of labelling (Figures 2C,F and S5–S7, Tables S3 and S4).

3.3. IAV Infection Reduces Membrane Protein Dynamics

Next, we aimed to determine whether the changes induced by IAV infection in the context of PM physical properties (see previous paragraphs) and lipid composition [6,7,9,22] have an effect on the diffusive dynamics of trans-membrane proteins. Therefore, we quantified the in-plane diffusion of three membrane(-associated) proteins: (i) a model for a protein associated with the inner leaflet of the PM (mp-mEGFP), (ii) a model for a protein associated with the outer leaflet of the PM (GPI-mEGFP) and (iii) a model of a trans-membrane protein (HA-mEGFP). Measurements were carried out in non-infected and FPV-/WSN-infected (16 hpi) HEK293T and DF1 cells. Quantification of the diffusion dynamics of the fluorescently labelled proteins was performed via sFCS measurements perpendicular to the membrane, at the equatorial plane of the cells. Representative cell images and ACFs obtained in HEK293T cells are shown in Figures S8 and S9, respectively.

Quantitative analysis of the ACFs indicated that both membrane-associated proteins diffuse in the PM of non-infected cells with a diffusion coefficient (D) of $\approx$1.1 μm^2/s, while the transmembrane protein exhibit slower dynamics (D $\approx$ 0.4 μm^2/s, Figure 3, Table S5). Both results are in line with previous experiments [46,56,79]. In FPV- and WSN-infected cells, we observed a decrease of diffusive dynamics for both mp-mEGFP (2.05-fold change $\pm$ 0.24) and GPI-mEGFP (1.81-fold change $\pm$ 0.15), for both cell lines. A decrease of mobility for the model transmembrane protein, HA-mEGFP, was also observed, albeit smaller (1.37-fold $\pm$ 0.23) and only in avian DF1 cells infected with either IAV strain.
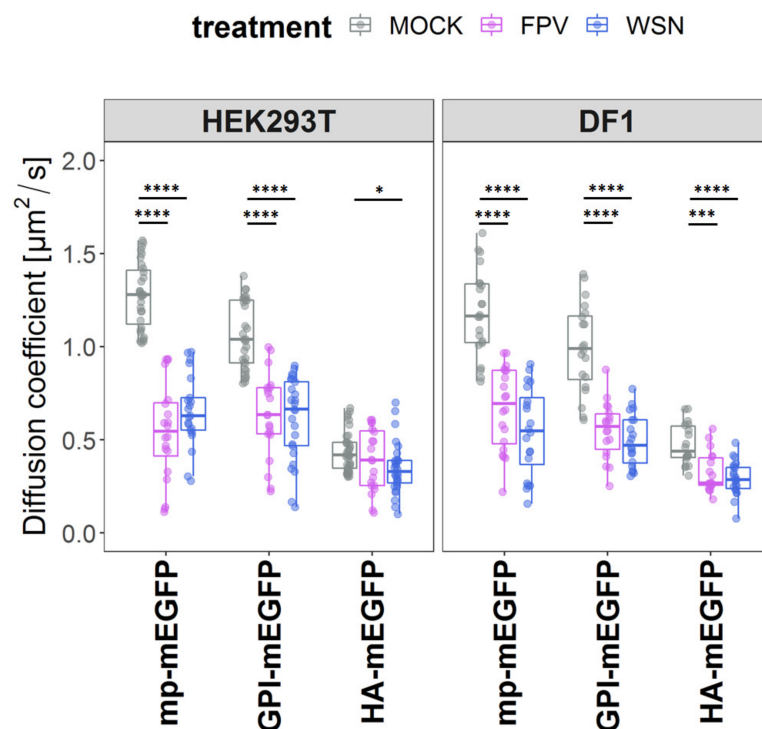

Figure 3. Decrease of membrane protein diffusion upon IAV-infection. Quantitative analysis of protein diffusion via fluorescence correlation spectroscopy (sFCS) in non-infected (MOCK) and

FPV-/WSN-infected HEK293T and DF1 cells expressing three model proteins labelled with green fluorescent proteins (mEGFPs) and associated with the plasma membrane (PM). Specifically, we investigated (i) a construct anchored to the inner leaflet of the PM via a myristoylated and palmitoylated (mp) peptide (mp-mEGFP), (ii) a construct anchored to the outer leaflet of the PM via a glycosylphosphatidylinositol (GPI) anchor (GPI-mEGFP), and (iii) one representative transmembrane protein, i.e., the influenza envelope protein hemagglutinin (HA-mEGFP). Measurements were performed at 16 hpi. The box plots show the diffusion coefficients calculated from sFCS diffusion times. Data from three separate experiments were plotted and analyzed using one-way ANOVA Tukey´s multiple comparison test (* $p < 0.05$, *** $p < 0.001$, **** $p < 0.0001$). Each data point represents the value measured at the PM in one cell (Table S5).

4. Discussion

Previous studies have shown that IAV infection induces changes in the lipid metabolism of infected cells [6,7,9]. Therefore, the concentration of specific lipids in cellular membranes might change as a consequence of infection [6,7,9]. For example, an IAV-induced increase in saturated lipids [5–7], cholesterol/sphingolipids [6,7,9] or anionic lipids [7,9] might significantly alter the physical properties of the PM, including local order of the lipid bilayer and its surface charge at the inner leaflet side. Such alterations, in turn, might affect protein–protein and protein–lipid interactions [80]. Here, we have quantified the effect of IAV infection on the properties of the PM and, specifically, its fluidity, structural order, and surface charge.

One finding of this study is the enhancement of the negative surface electrostatic potential at the inner leaflet of the PM, upon IAV infection, as demonstrated using a FRET-based membrane charge sensor. The simplest explanation for this result is an increase of the local concentration of anionic lipids in the inner leaflet. This idea is supported by the fact that the concentration of, e.g., PS in the membranes of infected cells or in the viral envelope was shown to be higher than in non-infected cells [5,7,9,21]. On the other hand, it must be kept in mind that our results might also be compatible with the electrostatic potential being altered by, e.g., changes in cytoplasm ionic strength/composition or, more likely, alterations in lipid/protein lateral organization [31,44]. In the latter case, it is reasonable that clustering of negative lipids or unbinding of positively charged proteins interacting with anionic lipids might alter the (local) effective electrostatic potential. In any case, such an increase in the amount or "availability" of anionic lipids at the inner leaflet might indeed relate to the organization of several viral components. For instance, it was shown that M1 is recruited by M2 to the PM and that M1 co-clusters with PS as well as with PIP2 [32,44,46]. Similar observations were made in the case of HA and both proteins contain polybasic residues which play a role in their interaction with anionic lipids and membrane localization [31,44,45]. Additionally, viral protein transport occurs via LC3, a protein that interacts with anionic lipids, especially in IAV-infected cells [41–43]. Finally, also genome packing is regulated by anionic lipids at the PM (i.e., PIP2) interacting with viral RNA and the IAV nucleoprotein NP [81].

Overall, these observations suggest that alterations in the local concentration of anionic lipid at the inner leaflet or, more in general, alterations of the negative electrostatic potential of infected cells might modulate viral assembly and release. Our results show for the first time that such alterations are indeed directly observable at the PM of infected cells, independent of IAV strain or cell type. Of note, this might be a general phenomenon, common also to other viral infections. For example, reduction in PS and PIP2 levels in mammalian cells hinders the recruitment of VP40 protein to the PM and its oligomerization, thereby inhibiting Ebola virus/Marburg virus assembly and egress (reviewed in [82]). Rearrangements of lipids at the PM, such as PIP2 and cholesterol, were also observed during the assembly of the human immunodeficiency virus (HIV) Gag protein (reviewed in [82]).

Another finding reported in this work is the enhancement of lipid–lipid interactions in the PM of infected cells. Specifically, we have used Laurdan and Di-4-ANEPPDHQ to

quantify the impact of IAV infection on membrane fluidity and lipid packing. These two fluorophores are commonly used to probe membrane order [50,51,58,78] and are influenced, each in a specific way, by several factors including cholesterol content (in connection to glycerol backbone dynamics), membrane hydration (in connection to lipid internal motions and hydrogen bond network dynamics) [77,83] and lipid phase behavior [50,78]. Furthermore, it has been reported that while Laurdan is a reliable probe for membrane order, Di-4-ANEPPDHQ is influenced by cholesterol and membrane potential [50]. Interestingly, our results indicate that both probes report similar alterations in the PM of IAV-infected cells. Taking into account previous lipidomic analyses [6,7,9] as well, the simplest explanation for these data is indeed an increase in the (local) concentration of cholesterol and/or saturated lipids (including, e.g., sphingolipids). Of interest, this interpretation is compatible with our results regarding the possible increase of negatively charged lipids: on one hand, an increase in cholesterol can be accompanied by higher levels of the anionic lipid PIP2 in cellular membranes (reviewed in [84]); on the other hand, a recent report linked the presence of PS to enhanced interleaflet coupling in model membranes and, as a consequence, an increase in membrane stiffness [85]. Furthermore, an increase in PM cholesterol concentration might at least partially explain the enhanced M2 clustering (see Figure S2, and compared to transfected cells [46]) which is, in fact, modulated by cholesterol [35,39,40]. This issue is the object of current studies in our laboratory.

As a consequence of the altered lipid composition and increased structural order, the diffusive dynamics of membrane components might be hindered. The in-plane mobility of transmembrane proteins is tightly connected to their function [86] and affects several cellular processes [87]. To study membrane dynamics in infected cells, we used two model fluorescent proteins associating with the inner leaflet of the PM (mp-mEGFP) or to its outer leaflet (*GPI*-mEGFP). Both markers diffused significantly slower after infection, in agreement with the increased membrane order that was detected upon infection, via, e.g., Laurdan-based assays. This effect was even stronger at later infection time points. The decreased fluidity of both leaflets might be due to alterations of either local lipid composition (i.e., restricted to one specific leaflet and transmitted to the other leaflet through enhanced interleaflet coupling [85,88]) or general bilayer composition (e.g., cholesterol concentration, affecting both leaflets [88]). Interestingly, the effect of infection on the diffusion dynamics of HA was less pronounced than for the other test proteins. This could be due to the fact that the diffusive dynamics of transmembrane proteins are determined also by other factors, such as interaction with the cytoskeleton, rather than just lipid bilayer viscosity [89–91]. Moreover, in the case of HA, it might be possible that this protein is enriched in specific domains [27,30,92] with a local lipid composition which is not significantly altered during infection. Nevertheless, our findings indicate that the diffusive dynamics of membrane-associated proteins are hindered in general by the decrease in membrane fluidity and/or increase in lipid packing. In general, such alterations in the membrane order parameters might originate from an overall re-organization of the membrane components or might be caused by the presence of, e.g., locally ordered membrane domains [11] from which the virus can efficiently assemble and bud.

Although our study focuses on the consequences of the increased lipid–lipid interactions in the PM of infected cells, it is interesting to speculate about the possible mechanisms leading to, e.g., alterations in membrane compositions during IAV infection. So far, the viral proteins, NA and M2, have been reported to directly alter the fatty acid metabolism of host cells [93]. Additionally, it appears that HA and NA are transported to the PM via cholesterol-/sphingomyelin-rich vesicles that might alter the composition of the target membrane [13,15,18,20,21,25]. Of interest, enrichment of cholesterol and saturated ordered-inducing lipids at the PM (or, specifically, at the budding site) might be important for the environmental stability of the virus and virus morphology [23,24,94,95].

5. Conclusions

In this study, we have provided evidence for IAV-induced alterations of PM dynamics and structural organization in infected cells. To the best of our knowledge, we demonstrate for the first time that IAV infection induces a decrease in membrane fluidity, an increase in lipid packing, and an enhancement of the negative electrostatic potential at the PM inner leaflet (probably caused by increased local concentrations of anionic lipids). Moreover, our study highlights the potential of combined biophysical methods to investigate membrane properties at the single-cell level, from multiple points of view, with the aim of better understanding virus–host interactions. These techniques can also be utilized in future studies to explore the effects of specific agents targeting lipid metabolism and host cell PM properties on virus egress and replication. Additionally, it might be possible to shed light on the role of specific viral proteins that influence membrane physical properties during virus assembly.

Supplementary Materials: The following supporting information can be downloaded at: https://www.mdpi.com/article/10.3390/v15091830/s1, Supporting Materials and Methods [96–98], Table S1: Overview of the Annexin V, cell viability and infection status analysis for HEK293T and DF1 cells, Table S2: Overview of the *RG* ratio from the FRET analysis for HEK293T and DF1 cells, Table S3: Overview of the *GP* index analysis with Laurdan for HEK293T and DF1 cells, Table S4: Overview of the *GP* index analysis with Di-4-ANEPPDHQ for HEK293T and DF1 cells, Table S5: Overview of the diffusion coefficient values [$\mu m^2/s$] from the sFCS analysis for HEK293T and DF1 cells, Figure S1: Schematic overview of the experimental setup for the analysis of the enrichment of negatively charged lipids at the inner leaflet of the PM via FRET (A,B), changes in membrane fluidity via *GP* index (C–E), and diffusion time of PM-associated proteins using sFCS (F-G) [99–102], Figure S2: No induction of apoptosis or PS flip upon FPV or WSN infection in human and avian cells, Figure S3: Quantification of the *RG* ratio from the FRET measurements at the PM of HEK293T and DF1 cells, Figure S4: *GP* and spectral phasor analysis of Laurdan- and Di-4-ANEPPDHQ-labelled GUVs, Figure S5: Spectral phasor analysis of Laurdan- and Di-4-ANEPPDHQ-labelled HEK293T and DF1 cells, Figure S6: Quantification of the *GP* index from the membrane fluidity measurements at the PM of HEK293T and DF1 cells with Laurdan and Di-4-ANEPPDHQ, Figure S7: The observed differences in RG ratio or GP index values do not depend on the amount of fluorophore, Figure S8: Representative confocal fluorescence images of HEK293T cells expressing mEGFP-tagged proteins, Figure S9: Examples of autocorrelation functions, Data S1: Excel sheet including data for Figures 1A,C, 2A,C,D,F, 3, S2C–E and S4A.

Author Contributions: Conceptualization, A.P.; methodology, A.P.; software, A.P. and S.C.; validation, A.P.; investigation, A.P.; writing—original draft preparation, A.P.; writing—review and editing, S.C.; visualization, A.P.; supervision, S.C.; project administration, S.C.; Funding Acquisition, S.C. All authors have read and agreed to the published version of the manuscript.

Institutional Review Board Statement: Not applicable.

Informed Consent Statement: Not applicable.

Data Availability Statement: The datasets analyzed during the current study are included the Supplementary Materials.

Conflicts of Interest: The authors declare no conflict of interest.

References

1. Tam, V.C.; Quehenberger, O.; Oshassnsky, C.M.; Suen, R.; Armando, A.M.; Treuting, P.M.; Thomas, P.G.; Dennis, E.A.; Aderem, A. Lipidomic Profiling of Influenza Infection Identifies Mediators that Induce and Resolve Inflammation. *Cell* **2013**, *154*, 213–227. [CrossRef]
2. Taubenberger, J.K.; Kash, J.C. Influenza virus evolution, host adaptation, and pandemic formation. *Cell Host Microbe* **2010**, *7*, 440–451. [CrossRef]

3. Schrauwen, E.J.A.; Fouchier, R.A.M. Host adaptation and transmission of influenza A viruses in mammals. *Emerg. Microbes Infect.* **2014**, *3*, e9. [CrossRef]

4. Cui, L.; Zheng, D.; Lee, Y.H.; Chan, T.K.; Kumar, Y.; Ho, W.E.; Chen, J.Z.; Tannenbaum, S.R.; Ong, C.N. Metabolomics Investigation Reveals Metabolite Mediators Associated with Acute Lung Injury and Repair in a Murine Model of Influenza Pneumonia. *Sci. Rep.* **2016**, *6*, 26076. [CrossRef] [PubMed]

5. Ivanova, P.T.; Myers, D.S.; Milne, S.B.; McClaren, J.L.; Thomas, P.G.; Brown, H.A. Lipid composition of viral envelope of three strains of influenza virus—Not all viruses are created equal. *ACS Infect. Dis.* **2015**, *1*, 399–452. [CrossRef]

6. Lin, S.; Liu, N.; Yang, Z.; Song, W.; Wang, P.; Chen, H.; Lucio, M.; Schmitt-Kopplin, P.; Chen, G.; Cai, Z. GC/MS-based metabolomics reveals fatty acid biosynthesis and cholesterol metabolism in cell lines infected with influenza A virus. *Talanta* **2010**, *83*, 262–268. [CrossRef] [PubMed]

7. Tanner, L.B.; Chng, C.; Guan, X.L.; Lei, Z.; Rozen, S.G.; Wenk, M.R. Lipidomics identifies a requirement for peroxisomal function during influenza virus replication. *J. Lipid Res.* **2014**, *55*, 1357–1365. [CrossRef]

8. Tisoncik-Go, J.; Gasper, D.J.; Kyle, J.E.; Eisfeld, A.J.; Selinger, C.; Hatta, M.; Morrison, J.; Korth, M.J.; Zink, E.M.; Kim, Y.M.; et al. Integrated Omics Analysis of Pathogenic Host Responses during Pandemic H1N1 Influenza Virus Infection: The Crucial Role of Lipid Metabolism. *Cell Host Microbe* **2016**, *19*, 254–266. [CrossRef]

9. Woods, P.S.; Doolittle, L.M.; Rosas, L.E.; Joseph, L.M.; Calomeni, E.P.; Davis, I.C. Lethal H1N1 influenza A virus infection alters the murine alveolar type II cell surfactant lipidome. *Am. J. Physiol.-Lung Cell. Mol. Physiol.* **2016**, *311*, L1160–L1169. [CrossRef]

10. Knepper, J.; Schierhorn, K.L.; Becher, A.; Budt, M.; Tönnies, M.; Bauer, T.T.; Schneider, P.; Neudecker, J.; Rückert, J.C.; Gruber, A.D.; et al. The novel human influenza A(H7N9) virus is naturally adapted to efficient growth in human lung tissue. *mBio* **2013**, *4*, e00601-13. [CrossRef] [PubMed]

11. Li, Y.-J.; Chen, C.-Y.; Yang, J.-H.; Chiu, Y.-F. Modulating cholesterol-rich lipid rafts to disrupt influenza A virus infection. *Front. Immunol.* **2022**, *13*, 982264. [CrossRef] [PubMed]

12. Wang, D.; Zhu, W.; Yang, L.; Shu, Y. The Epidemiology, Virology, and Pathogenicity of Human Infections with Avian Influenza Viruses. *Cold Spring Harb. Perspect. Med.* **2021**, *11*, a038620. [CrossRef] [PubMed]

13. Audi, A.; Soudani, N.; Dbaibo, G.; Zaraket, H. Depletion of Host and Viral Sphingomyelin Impairs Influenza Virus Infection. *Front. Microbiol.* **2020**, *11*, 612. [CrossRef] [PubMed]

14. Hidari, K.I.P.J.; Suzuki, Y.; Suzuki, T. Suppression of the Biosynthesis of Cellular Sphingolipids Results in the Inhibition of the Maturation of Influenza Virus Particles in MDCK Cells. *Biol. Pharm. Bull.* **2006**, *29*, 1575–1579. [CrossRef]

15. Ohkura, T.; Momose, F.; Ichikawa, R.; Takeuchi, K.; Morikawa, Y. Influenza A virus hemagglutinin and neuraminidase mutually accelerate their apical targeting through clustering of lipid rafts. *J. Virol.* **2014**, *88*, 10039–10055. [CrossRef]

16. Rossman, J.S.; Lamb, R.A. Influenza virus assembly and budding. *Virology* **2011**, *411*, 229–236. [CrossRef]

17. Tafesse, F.G.; Sanyal, S.; Ashour, J.; Guimaraes, C.P.; Hermansson, M.; Somerharju, P.; Ploegh, H.L. Intact sphingomyelin biosynthetic pathway is essential for intracellular transport of influenza virus glycoproteins. *Proc. Natl. Acad. Sci. USA* **2013**, *110*, 6406–6411. [CrossRef]

18. Sato, R.; Okura, T.; Kawahara, M.; Takizawa, N.; Momose, F.; Morikawa, Y. Apical Trafficking Pathways of Influenza A Virus HA and NA via Rab17- and Rab23-Positive Compartments. *Front. Microbiol.* **2019**, *10*, 1857. [CrossRef]

19. Scheiffele, P.; Rietveld, A.; Wilk, T.; Simons, K. Influenza viruses select ordered lipid domains during budding from the plasma membrane. *J. Biol. Chem.* **1999**, *274*, 2038–2044. [CrossRef]

20. Veit, M.; Thaa, B. Association of influenza virus proteins with membrane rafts. *Adv. Virol.* **2011**, *2011*, 370606. [CrossRef]

21. Zhang, J.; Pekosz, A.; Lamb, R.A. Influenza virus assembly and lipid raft microdomains: A role for the cytoplasmic tails of the spike glycoproteins. *J. Virol.* **2000**, *74*, 4634–4644. [CrossRef]

22. Gerl, M.J.; Sampaio, J.L.; Urban, S.; Kalvodova, L.; Verbavatz, J.M.; Binnington, B.; Lindemann, D.; Lingwood, C.A.; Shevchenko, A.; Schroeder, C.; et al. Quantitative analysis of the lipidomes of the influenza virus envelope and MDCK cell apical membrane. *J. Cell Biol.* **2012**, *196*, 213–221. [CrossRef]

23. Barman, S.; Nayak, D.P. Lipid raft disruption by cholesterol depletion enhances influenza A virus budding from MDCK cells. *J. Virol.* **2007**, *81*, 12169–12178. [CrossRef]

24. Rossman, J.S.; Jing, X.; Leser, G.P.; Balannik, V.; Pinto, L.H.; Lamb, R.A. Influenza virus m2 ion channel protein is necessary for filamentous virion formation. *J. Virol.* **2010**, *84*, 5078–5088. [CrossRef]

25. Barman, S.; Nayak, D.P. Analysis of the transmembrane domain of influenza virus neuraminidase, a type II transmembrane glycoprotein, for apical sorting and raft association. *J. Virol.* **2000**, *74*, 6538–6545. [CrossRef]

26. Engel, S.; de Vries, M.; Herrmann, A.; Veit, M. Mutation of a raft-targeting signal in the transmembrane region retards transport of influenza virus hemagglutinin through the Golgi. *FEBS Lett.* **2012**, *586*, 277–282. [CrossRef]

27. Wilson, R.L.; Frisz, J.F.; Klitzing, H.A.; Zimmerberg, J.; Weber, P.K.; Kraft, M.L. Hemagglutinin Clusters in the Plasma Membrane Are Not Enriched with Cholesterol and Sphingolipids. *Biophys. J.* **2015**, *108*, 1652–1659. [CrossRef]

28. Leser, G.P.; Lamb, R.A. Lateral Organization of Influenza Virus Proteins in the Budozone Region of the Plasma Membrane. *J. Virol.* **2017**, *91*, e02104-16. [CrossRef]

29. Leser, G.P.; Lamb, R.A. Influenza virus assembly and budding in raft-derived microdomains: A quantitative analysis of the surface distribution of HA, NA and M2 proteins. *Virology* **2005**, *342*, 215–227. [CrossRef]

30. Veit, M.; Engel, S.; Thaa, B.; Scolari, S.; Herrmann, A. Lipid domain association of influenza virus proteins detected by dynamic fluorescence microscopy techniques. *Cell. Microbiol.* **2013**, *15*, 179–189. [CrossRef]

31. Curthoys, N.M.; Mlodzianoski, M.J.; Parent, M.; Butler, M.B.; Raut, P.; Wallace, J.; Lilieholm, J.; Mehmood, K.; Maginnis, M.S.; Waters, H.; et al. Influenza Hemagglutinin Modulates Phosphatidylinositol 4,5-Bisphosphate Membrane Clustering. *Biophys. J.* **2019**, *116*, 893–909. [CrossRef]

32. Raut, P.; Obeng, B.; Waters, H.; Zimmerberg, J.; Gosse, J.A.; Hess, S.T. Phosphatidylinositol 4,5-Bisphosphate Mediates the Co-Distribution of Influenza A Hemagglutinin and Matrix Protein M1 at the Plasma Membrane. *Viruses* **2022**, *14*, 2509. [CrossRef]

33. Ekanayake, E.V.; Fu, R.; Cross, T.A. Structural Influences: Cholesterol, Drug, and Proton Binding to Full-Length Influenza A M2 Protein. *Biophys. J.* **2016**, *110*, 1391–1399. [CrossRef] [PubMed]

34. Elkins, M.R.; Williams, J.K.; Gelenter, M.D.; Dai, P.; Kwon, B.; Sergeyev, I.V.; Pentelute, B.L.; Hong, M. Cholesterol-binding site of the influenza M2 protein in lipid bilayers from solid-state NMR. *Proc. Natl. Acad. Sci. USA* **2017**, *114*, 12946–12951. [CrossRef] [PubMed]

35. Georgieva, E.R.; Borbat, P.P.; Norman, H.D.; Freed, J.H. Mechanism of influenza A M2 transmembrane domain assembly in lipid membranes. *Sci. Rep.* **2015**, *5*, 11757. [CrossRef] [PubMed]

36. Kuroki, T.; Hatta, T.; Natsume, T.; Sakai, N.; Yagi, A.; Kato, K.; Nagata, K.; Kawaguchi, A. ARHGAP1 Transported with Influenza Viral Genome Ensures Integrity of Viral Particle Surface through Efficient Budozone Formation. *mBio* **2022**, *13*, e0072122. [CrossRef]

37. Manzoor, R.; Igarashi, M.; Takada, A. Influenza A Virus M2 Protein: Roles from Ingress to Egress. *Int. J. Mol. Sci.* **2017**, *18*, 2649. [CrossRef]

38. Martyna, A.; Bahsoun, B.; Madsen, J.J.; Jackson, F.; Badham, M.D.; Voth, G.A.; Rossman, J.S. Cholesterol Alters the Orientation and Activity of the Influenza Virus M2 Amphipathic Helix in the Membrane. *J. Phys. Chem. B* **2020**, *124*, 6738–6747. [CrossRef] [PubMed]

39. Paulino, J.; Pang, X.; Hung, I.; Zhou, H.X.; Cross, T.A. Influenza A M2 Channel Clustering at High Protein/Lipid Ratios: Viral Budding Implications. *Biophys. J.* **2019**, *116*, 1075–1084. [CrossRef] [PubMed]

40. Sutherland, M.; Tran, N.; Hong, M. Clustering of tetrameric influenza M2 peptides in lipid bilayers investigated by (19)F solid-state NMR. *Biochim. Biophys. Acta Biomembr.* **2022**, *1864*, 183909. [CrossRef]

41. Beale, R.; Wise, H.; Stuart, A.; Ravenhill, B.J.; Digard, P.; Randow, F. A LC3-interacting motif in the influenza A virus M2 protein is required to subvert autophagy and maintain virion stability. *Cell Host Microbe* **2014**, *15*, 239–247. [CrossRef]

42. Dunsing, V.; Petrich, A.; Chiantia, S. Multicolor fluorescence fluctuation spectroscopy in living cells via spectral detection. *Elife* **2021**, *10*, e69687. [CrossRef] [PubMed]

43. Durgan, J.; Florey, O. Many roads lead to CASM: Diverse stimuli of noncanonical autophagy share a unifying molecular mechanism. *Sci. Adv.* **2022**, *8*, eabo1274. [CrossRef] [PubMed]

44. Bobone, S.; Hilsch, M.; Storm, J.; Dunsing, V.; Herrmann, A.; Chiantia, S. Phosphatidylserine Lateral Organization Influences the Interaction of Influenza Virus Matrix Protein 1 with Lipid Membranes. *J. Virol.* **2017**, *91*, e00267-17. [CrossRef] [PubMed]

45. Kordyukova, L.V.; Shtykova, E.V.; Baratova, L.A.; Svergun, D.I.; Batishchev, O.V. Matrix proteins of enveloped viruses: A case study of Influenza A virus M1 protein. *J. Biomol. Struct. Dyn.* **2019**, *37*, 671–690. [CrossRef]

46. Petrich, A.; Dunsing, V.; Bobone, S.; Chiantia, S. Influenza A M2 recruits M1 to the plasma membrane: A fluorescence fluctuation microscopy study. *Biophys. J.* **2021**, *120*, 5478–5490. [CrossRef]

47. Zhou, Y.; Pu, J.; Wu, Y. The Role of Lipid Metabolism in Influenza A Virus Infection. *Pathogens* **2021**, *10*, 303. [CrossRef]

48. Kawaguchi, A.; Hirohama, M.; Harada, Y.; Osari, S.; Nagata, K. Influenza Virus Induces Cholesterol-Enriched Endocytic Recycling Compartments for Budozone Formation via Cell Cycle-Independent Centrosome Maturation. *PLoS Pathog.* **2015**, *11*, e1005284. [CrossRef]

49. Ma, Y.; Yamamoto, Y.; Nicovich, P.R.; Goyette, J.; Rossy, J.; Gooding, J.J.; Gaus, K. A FRET sensor enables quantitative measurements of membrane charges in live cells. *Nat. Biotechnol.* **2017**, *35*, 363–370. [CrossRef]

50. Amaro, M.; Reina, F.; Hof, M.; Eggeling, C.; Sezgin, E. Laurdan and Di-4-ANEPPDHQ probe different properties of the membrane. *J. Phys. D Appl. Phys.* **2017**, *50*, 134004. [CrossRef]

51. Owen, D.M.; Rentero, C.; Magenau, A.; Abu-Siniyeh, A.; Gaus, K. Quantitative imaging of membrane lipid order in cells and organisms. *Nat. Protoc.* **2011**, *7*, 24–35. [CrossRef] [PubMed]

52. Chiantia, S.; Ries, J.; Schwille, P. Fluorescence correlation spectroscopy in membrane structure elucidation. *Biochim. Biophys. Acta* **2009**, *1788*, 225–233. [CrossRef] [PubMed]

53. Dunsing, V.; Chiantia, S. A Fluorescence Fluctuation Spectroscopy Assay of Protein-Protein Interactions at Cell-Cell Contacts. *JoVE* **2018**, *142*, e58582. [CrossRef]

54. Tzoneva, R.; Stoyanova, T.; Petrich, A.; Popova, D.; Uzunova, V.; Momchilova, A.; Chiantia, S. Effect of Erufosine on Membrane Lipid Order in Breast Cancer Cell Models. *Biomolecules* **2020**, *10*, 802. [CrossRef] [PubMed]

55. Yang, G.-S.; Wagenknecht-Wiesner, A.; Yin, B.; Suresh, P.; London, E.; Baird, B.; Bag, N. Lipid Driven Inter-leaflet Coupling of Plasma Membrane Order Regulates FcεRI Signaling in Mast Cells. *Biophys. J.* **2023**. Online ahead of print. [CrossRef]

56. Dunsing, V.; Luckner, M.; Zühlke, B.; Petazzi, R.A.; Herrmann, A.; Chiantia, S. Optimal fluorescent protein tags for quantifying protein oligomerization in living cells. *Sci. Rep.* **2018**, *8*, 10634. [CrossRef]

57. Wagner, R.; Gabriel, G.; Schlesner, M.; Alex, N.; Herwig, A.; Werner, O.; Klenk, H.-D. Protease activation mutants elicit protective immunity against highly pathogenic avian influenza viruses of subtype H7 in chickens and mice. *Emerg. Microbes Infect.* **2013**, *2*, e7. [CrossRef]

58. Sezgin, E.; Waithe, D.; Bernardino de la Serna, J.; Eggeling, C. Spectral imaging to measure heterogeneity in membrane lipid packing. *Chemphyschem* **2015**, *16*, 1387–1394. [CrossRef]

59. Petrich, A.; Koikkarah Aji, A.; Dunsing, V.; Chiantia, S. Benchmarking of novel green fluorescent proteins for the quantification of protein oligomerization in living cells. *PLoS ONE* **2023**, *18*, e0285486. [CrossRef]

60. Petrášek, Z.; Schwille, P. Precise Measurement of Diffusion Coefficients using Scanning Fluorescence Correlation Spectroscopy. *Biophys. J.* **2008**, *94*, 1437–1448. [CrossRef]

61. Ries, J.; Chiantia, S.; Schwille, P. Accurate determination of membrane dynamics with line-scan FCS. *Biophys. J.* **2009**, *96*, 1999–2008. [CrossRef]

62. Ries, J.; Schwille, P. Studying Slow Membrane Dynamics with Continuous Wave Scanning Fluorescence Correlation Spectroscopy. *Biophys. J.* **2006**, *91*, 1915–1924. [CrossRef]

63. Liu, S.; Mok, B.W.-Y.; Deng, S.; Liu, H.; Wang, P.; Song, W.; Chen, P.; Huang, X.; Zheng, M.; Lau, S.-Y.; et al. Mammalian cells use the autophagy process to restrict avian influenza virus replication. *Cell Rep.* **2021**, *35*, 109213. [CrossRef]

64. Chaurio, R.A.; Janko, C.; Muñoz, L.E.; Frey, B.; Herrmann, M.; Gaipl, U.S. Phospholipids: Key Players in Apoptosis and Immune Regulation. *Molecules* **2009**, *14*, 4892–4914. [CrossRef]

65. Gui, R.; Chen, Q. Molecular Events Involved in Influenza A Virus-Induced Cell Death. *Front. Microbiol.* **2021**, *12*, 797789. [CrossRef]

66. Bailey, R.W.; Nguyen, T.; Robertson, L.; Gibbons, E.; Nelson, J.; Christensen, R.E.; Bell, J.P.; Judd, A.M.; Bell, J.D. Sequence of Physical Changes to the Cell Membrane During Glucocorticoid-Induced Apoptosis in S49 Lymphoma Cells. *Biophys. J.* **2009**, *96*, 2709–2718. [CrossRef]

67. Darwich, Z.; Klymchenko, A.S.; Kucherak, O.A.; Richert, L.; Mély, Y. Detection of apoptosis through the lipid order of the outer plasma membrane leaflet. *Biochim. Biophys. Acta* **2012**, *1818*, 3048–3054. [CrossRef]

68. Tochigi, M.; Inoue, T.; Suzuki-Karasaki, M.; Ochiai, T.; Ra, C.; Suzuki-Karasaki, Y. Hydrogen peroxide induces cell death in human TRAIL-resistant melanoma through intracellular superoxide generation. *Int. J. Oncol.* **2013**, *42*, 863–872. [CrossRef]

69. Wu, C.A.; Yang, Y.W. Induction of cell death by saponin and antigen delivery. *Pharm. Res.* **2004**, *21*, 271–277. [CrossRef]

70. Leavesley, S.J.; Britain, A.L.; Cichon, L.K.; Nikolaev, V.O.; Rich, T.C. Assessing FRET using spectral techniques. *Cytom. Part A* **2013**, *83*, 898–912. [CrossRef]

71. Pokorna, S.; Ventura, A.E.; Santos, T.C.B.; Hof, M.; Prieto, M.; Futerman, A.H.; Silva, L.C. Laurdan in live cell imaging: Effect of acquisition settings, cell culture conditions and data analysis on generalized polarization measurements. *J. Photochem. Photobiol. B* **2022**, *228*, 112404. [CrossRef]

72. Fellmann, P.; Hervé, P.; Pomorski, T.; Müller, P.; Geldwerth, D.; Herrmann, A.; Devaux, P.F. Transmembrane movement of diether phospholipids in human erythrocytes and human fibroblasts. *Biochemistry* **2000**, *39*, 4994–5003. [CrossRef]

73. Herrera, S.A.; Grifell-Junyent, M.; Pomorski, T.G. NBD-lipid Uptake Assay for Mammalian Cell Lines. *Bio-Protocol* **2022**, *12*, e4330. [CrossRef]

74. Klenk, H.D.; Rott, R.; Becht, H. On the structure of the influenza virus envelope. *Virology* **1972**, *47*, 579–591. [CrossRef]

75. Landsberger, F.R.; Lenard, J.; Paxton, J.; Compans, R.W. Spin-labeled electron spin resonance study of the lipid-containing membrane of influenza virus. *Proc. Natl. Acad. Sci. USA* **1971**, *68*, 2579–2583. [CrossRef]

76. Golfetto, O.; Hinde, E.; Gratton, E. The Laurdan spectral phasor method to explore membrane micro-heterogeneity and lipid domains in live cells. *Methods Mol. Biol.* **2015**, *1232*, 273–290. [CrossRef]

77. Jin, L.; Millard, A.C.; Wuskell, J.P.; Dong, X.; Wu, D.; Clark, H.A.; Loew, L.M. Characterization and application of a new optical probe for membrane lipid domains. *Biophys. J.* **2006**, *90*, 2563–2575. [CrossRef]

78. Sezgin, E.; Sadowski, T.; Simons, K. Measuring lipid packing of model and cellular membranes with environment sensitive probes. *Langmuir* **2014**, *30*, 8160–8166. [CrossRef] [PubMed]

79. Dunsing, V.; Mayer, M.; Liebsch, F.; Multhaup, G.; Chiantia, S. Direct evidence of amyloid precursor-like protein 1 trans interactions in cell-cell adhesion platforms investigated via fluorescence fluctuation spectroscopy. *Mol. Biol. Cell* **2017**, *28*, 3609–3620. [CrossRef]

80. Goyette, J.; Gaus, K. Mechanisms of protein nanoscale clustering. *Curr. Opin. Cell Biol.* **2017**, *44*, 86–92. [CrossRef]

81. Kakisaka, M.; Yamada, K.; Yamaji-Hasegawa, A.; Kobayashi, T.; Aida, Y. Intrinsically disordered region of influenza A NP regulates viral genome packaging via interactions with viral RNA and host PI(4,5)P2. *Virology* **2016**, *496*, 116–126. [CrossRef]

82. Motsa, B.B.; Stahelin, R.V. Lipid-protein interactions in virus assembly and budding from the host cell plasma membrane. *Biochem. Soc. Trans.* **2021**, *49*, 1633–1641. [CrossRef]

83. Orlikowska-Rzeznik, H.; Krok, E.; Chattopadhyay, M.; Lester, A.; Piatkowski, L. Laurdan Discerns Lipid Membrane Hydration and Cholesterol Content. *J. Phys. Chem. B* **2023**, *127*, 3382–3391. [CrossRef]

84. Doole, F.T.; Gupta, S.; Kumarage, T.; Ashkar, R.; Brown, M.F. Biophysics of Membrane Stiffening by Cholesterol and Phosphatidylinositol 4,5-bisphosphate (PIP2). *Adv. Exp. Med. Biol.* **2023**, *1422*, 61–85. [CrossRef]

85. Frewein, M.P.K.; Piller, P.; Semeraro, E.F.; Czakkel, O.; Gerelli, Y.; Porcar, L.; Pabst, G. Distributing aminophospholipids asymmetrically across leaflets causes anomalous membrane stiffening. *Biophys. J.* **2023**, *122*, 2445–2455. [CrossRef]

86. Maynard, S.A.; Triller, A. Inhibitory Receptor Diffusion Dynamics. *Front. Mol. Neurosci.* **2019**, *12*, 313. [CrossRef]
87. Alenghat, F.J.; Golan, D.E. Membrane protein dynamics and functional implications in mammalian cells. *Curr. Top. Membr.* **2013**, *72*, 89–120. [CrossRef]
88. Sarmento, M.J.; Hof, M.; Šachl, R. Interleaflet Coupling of Lipid Nanodomains—Insights From in vitro Systems. *Front. Cell Dev. Biol.* **2020**, *8*, 284. [CrossRef]
89. Bag, N.; Huang, S.; Wohland, T. Plasma Membrane Organization of Epidermal Growth Factor Receptor in Resting and Ligand-Bound States. *Biophys. J.* **2015**, *109*, 1925–1936. [CrossRef] [PubMed]
90. Gudheti, M.V.; Curthoys, N.M.; Gould, T.J.; Kim, D.; Gunewardene, M.S.; Gabor, K.A.; Gosse, J.A.; Kim, C.H.; Zimmerberg, J.; Hess, S.T. Actin mediates the nanoscale membrane organization of the clustered membrane protein influenza hemagglutinin. *Biophys. J.* **2013**, *104*, 2182–2192. [CrossRef]
91. Huang, S.; Lim, S.Y.; Gupta, A.; Bag, N.; Wohland, T. Plasma membrane organization and dynamics is probe and cell line dependent. *Biochim. Biophys. Acta Biomembr.* **2017**, *1859*, 1483–1492. [CrossRef]
92. Frisz, J.F.; Lou, K.; Klitzing, H.A.; Hanafin, W.P.; Lizunov, V.; Wilson, R.L.; Carpenter, K.J.; Kim, R.; Hutcheon, I.D.; Zimmerberg, J.; et al. Direct chemical evidence for sphingolipid domains in the plasma membranes of fibroblasts. *Proc. Natl. Acad. Sci. USA* **2013**, *110*, E613–E622. [CrossRef]
93. Chua, S.; Cui, J.; Engelberg, D.; Lim, L.H.K. A Review and Meta-Analysis of Influenza Interactome Studies. *Front. Microbiol.* **2022**, *13*, 869406. [CrossRef]
94. Bajimaya, S.; Frankl, T.; Hayashi, T.; Takimoto, T. Cholesterol is required for stability and infectivity of influenza A and respiratory syncytial viruses. *Virology* **2017**, *510*, 234–241. [CrossRef]
95. Zeng, L.; Li, J.; Lv, M.; Li, Z.; Yao, L.; Gao, J.; Wu, Q.; Wang, Z.; Yang, X.; Tang, G.; et al. Environmental Stability and Transmissibility of Enveloped Viruses at Varied Animate and Inanimate Interfaces. *Environ. Health* **2023**, *1*, 15–31. [CrossRef] [PubMed]
96. Angelova, M.I.; Dimitrov, D.S. Liposome electroformation. *Faraday Discuss. Chem. Soc.* **1986**, *81*, 303–311. [CrossRef]
97. Stein, H.; Spindler, S.; Bonakdar, N.; Wang, C.; Sandoghdar, V. Production of Isolated Giant Unilamellar Vesicles under High Salt Concentrations. *Front. Physiol.* **2017**, *8*, 63. [CrossRef]
98. Malacrida, L.; Astrada, S.; Briva, A.; Bollati-Fogolín, M.; Gratton, E.; Bagatolli, L.A. Spectral phasor analysis of LAURDAN fluorescence in live A549 lung cells to study the hydration and time evolution of intracellular lamellar body-like structures. *Biochim. Biophys. Acta* **2016**, *1858*, 2625–2635. [CrossRef]
99. Klymchenko, A.S.; Kreder, R. Fluorescent probes for lipid rafts: From model membranes to living cells. *Chem. Biol.* **2014**, *21*, 97–113. [CrossRef]
100. Bondelli, G.; Sardar, S.; Chiaravalli, G.; Vurro, V.; Paternò, G.M.; Lanzani, G.; D'Andrea, C. Shedding Light on Thermally Induced Optocapacitance at the Organic Biointerface. *J. Phys. Chem. B* **2021**, *125*, 10748–10758. [CrossRef]
101. Gunther, G.; Malacrida, L.; Jameson, D.M.; Gratton, E.; Sánchez, S.A. LAURDAN since Weber: The Quest for Visualizing Membrane Heterogeneity. *Acc. Chem. Res.* **2021**, *54*, 976–987. [CrossRef] [PubMed]
102. Yu, L.; Lei, Y.; Ma, Y.; Liu, M.; Zheng, J.; Dan, D.; Gao, P. A Comprehensive Review of Fluorescence Correlation Spectroscopy. *Front. Phys.* **2021**, *9*, 644450. [CrossRef]